Magnetic Resonance in Medicine 45:29–35 (2001)

Superresolution in MRI: Application to Human White Matter Fiber Tract Visualization by Diffusion Tensor Imaging

Sharon Peled[1*] and Yehezkel Yeshurun[2]

A superresolution algorithm was applied to spatially shifted, single-shot, diffusion-weighted brain images to generate a new image with increased spatial resolution. Detailed two-dimensional white matter fiber tract maps of the human brain resulting from application of the technique are shown. The method provides a new means for improving the resolution in cases where *k*-space segmentation is difficult to implement. Diffusion-weighted imaging and diffusion tensor imaging in vivo stand to benefit in particular because the necessity of obtaining high-resolution scans is matched by the difficulty in obtaining them. Magn Reson Med 45:29–35, 2001. © 2001 Wiley-Liss, Inc.

Key words: high-resolution MRI; echo-planar imaging; white matter tractography in vivo; brain conductivity mapping; single-shot imaging

The term superresolution refers to image processing methods that increase spatial resolution by pooling information from a number of images. The original low-resolution images may be translated, blurred, rotated, or scaled. Superresolution techniques have been used, for example, for reconstructing an image from a few frames of a movie or from pictures taken by a moving satellite. We present the first useful application of superresolution to MRI, fusing spatially shifted, single-shot, diffusion-weighted images to create new images with improved resolution and finer detail. The method is easy to implement because it is based on an existing pulse sequence and a simple reconstruction algorithm. It is relatively insensitive to motion and does not require cardiac gating.

In most MRI pulse sequences, high spatial resolution is achieved by multi-shot acquisition of data, i.e., data collected after multiple RF excitations contribute to each image. If higher resolution is wished for, a larger area of "*k*-space" (Fourier transform of image space) is acquired—this usually means more excitations. The resolution of images acquired in this manner is limited by the imaging time available, and by the ability of the scanned subject to keep still. MRI pulse sequences vary in their degree of sensitivity to motion artifacts. Diffusion-weighted imaging (DWI), for example, is incompatible with such simple segmented *k*-space approaches due to the large phase variations resulting from even minimal physiological motion during the application of the field gradients necessary for diffusion weighting. Thus high-resolution DWI remains a challenge.

DWI has developed into an important MR method for neurological applications, particularly in the early detection of stroke (1,2). Improved resolution in apparent diffusion coefficient (ADC) maps may mean detection of smaller lesions. In addition to providing images of the ADC, DWI can be used to measure the spatial anisotropy of the diffusion in tissues whose structural characteristics can thus be probed (3). Diffusion tensor imaging (DTI) is a variation of DWI in which at least seven images are acquired for every slice, with at least six different directions of diffusion weighting. In the white matter of the brain, DTI provides a unique tool for visualization of the direction and intactness of white matter fiber tracts in vivo by identifying the preferred direction of diffusion (4).

Today there are three categories of methods for obtaining DWI (or DTI):

- The most popular diffusion imaging sequences are the ultrafast sequences, such as the diffusion-sensitized echo-planar imaging (EPI) technique (5), which acquire a complete image in one shot, thus avoiding phase problems. Other single-shot techniques, such as those based on RARE (6), and GRASE (7) acquisition schemes, could possibly also be modified to provide diffusion weighting. Single-shot techniques are inherently resolution limited for brain imaging.
- Methods employing navigator echoes (8). Complex motion, including physiological motion, cannot be fully corrected for using navigator echoes.
- Methods that can ignore phase inconsistencies between excitations by relying on reconstruction in image space and not in *k*-space. Examples are line scan diffusion imaging (9) and projection reconstruction (10,11). Line scan diffusion tensor imaging provides undistorted images but is an inherently slow and low-signal-to-noise ratio (SNR) technique (12). Methods based on projection reconstruction show promise but still require work on artifact reduction.

Our method of superresolution DTI is based on the combination in image space of a few shifted single-shot images.

High-resolution DTI, combined with algorithms for tracing fibers in three dimensions in tensor fields, has the potential to enable fiber tract mapping of critical functional pathways in the brain in vivo. Recently 3D white matter fiber tract reconstructions from DTI in the rat (13), and in the human (14–16), have been attempted. Another approach to fiber tracing, via *q*-space analysis (17,18), was recently applied (19) to diffusion data to find multiple

[1]Tel Aviv Sourasky Medical Center, Department of Radiology, Tel Aviv, Israel.
[2]Tel Aviv University, Department of Computer Science, Ramat Aviv, Tel Aviv, Israel.
*Correspondence to: Sharon Peled, Department of Radiology/MRI, Tel Aviv Sourasky Medical Center, 6 Weizman St., Tel Aviv 64239, Israel.
E-mail: speled@tasmc.health.gov.il
Received 5 July 2000; revised 22 September 2000; accepted 22 September 2000.

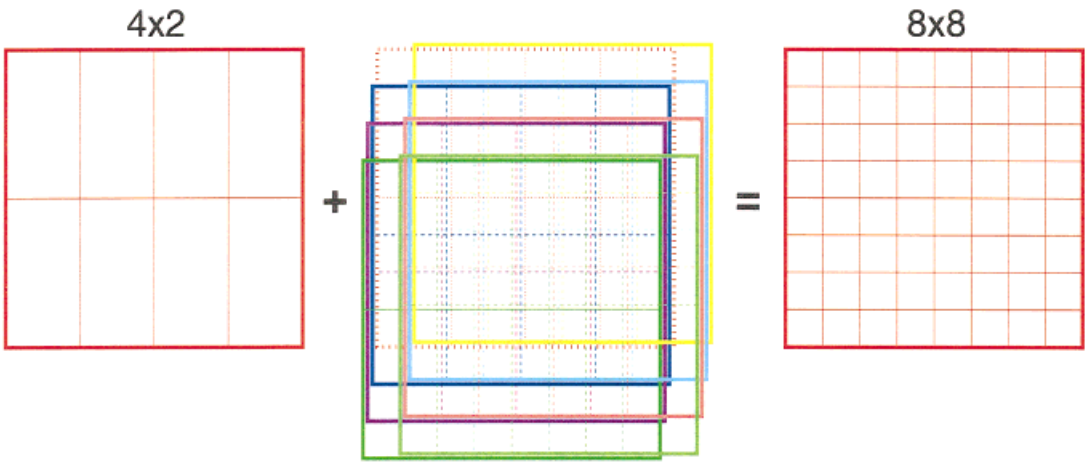

FIG. 1. Scheme of shifted image acquisition: eight images are acquired with subpixel spatial shifts.

white matter directions in each voxel. Currently partial voluming effects (averaging of multiple macroscopic environments in one voxel) pose a severe impediment to the analysis of directional and structural axonal connectivity (e.g., 2.5-mm voxel side in Ref. 14, 1.9 × 3.75 × 5 mm in Ref. 15, 1.9 × 1.9 × 2.8 mm in Ref. 16, and 4-mm voxel side in Ref. 19). The higher the spatial resolution of the attainable diffusion imaging data, the more relevant the endeavor of 3D fiber tract tracking will become and the more robust the algorithms for doing so will be.

A number of superresolution algorithms exist (20–24). We chose to use here, for demonstration purposes, the iterative back-projection (IBP) method of Irani and Peleg (20), and plan to perform rigorous comparisons between the different methods in the near future to find the most suitable one. The IBP method is based on the minimization of differences between the original low-resolution images, and the low-resolution images that can be generated (back-projected) from down-sampling the current best guess of the high-resolution image. The algorithm is simple to implement and converges rapidly.

Single-shot spin-echo EPI usually provides satisfactory images of the human brain with a matrix size of 128 × 64. Increasing the number of lines in the phase-encode direction reduces the SNR due to T_2^* decay. Higher resolution in the read-out direction increases the spatial distortions resulting from magnetic field inhomogeneity, as well as affecting the SNR. In an image field of view (FOV) of 256 mm, a matrix size of 128 × 64 translates to in-plane spatial resolution of 2 mm × 4 mm. For each image required for DTI analysis, we acquired eight of these lower-resolution images with sub-pixel shifts, and combined them using the IBP algorithm to obtain a nominal in-plane resolution of 1 mm^2. DTI analysis was then performed on the set of reconstructed high-resolution images.

METHODS

MRI Protocol

All images were acquired on a GE Horizon echospeed 1.5 Tesla MRI system using single-shot diffusion-weighted spin-echo EPI. No head restraint or cardiac gating was used. Basic imaging parameters were: TR = 2 sec, TE = 123 msec, FOV = 25.6 cm, matrix = 128 × 64 (in-plane resolution of 2 mm × 4 mm), effective BW of 88 kHz with ramp sampling, eight slices of 3-mm thickness. The low-resolution scan consisted of the acquisition of five dummy images to reach steady state, three low diffusion-weighted images in the cardinal directions, and six highly diffusion-weighted images (b-value of 1000, gradient pulse length 16.4 msec at 2.2 mT/m) in the directions [1,1,0], [1,0,1], [0,1,1], [1,−1,0], [1,0,−1], and [0,1,−1] (25). We used a long echo time with full k-space acquisition to avoid diffusion gradient direction-dependent distortions. The high b-value images were repeated six times to improve SNR. Scan time was $1\frac{1}{2}$ min. The low-resolution scan was repeated eight times, each scan with a shifted FOV, as shown in Fig. 1, to give a total imaging time of 12 min. Satisfactory results were also obtained without averaging, in which case the imaging time would have been 4 min for eight DTI slices.

The first four images were acquired with 0-, 1-, 2-, and 3-mm shifts in the phase-encode direction (0, $\frac{1}{4}$, $\frac{1}{2}$, $\frac{3}{4}$ pixel vertical shifts in Fig. 1), and then again all four shifts were acquired with an additional 1-mm shift in the frequency-encode direction (0, $\frac{1}{2}$ pixel horizontal shifts in Fig. 1).

For the phantom experiment, regular spin-echo EPI was used with matrix size = 64 × 64, FOV = 14 cm, BW = 62.5 kHz, and four image acquisition shifts of 1.1 mm ($\frac{1}{2}$ pixel).

Superresolution Image Enhancement

The method of Irani and Peleg (20) was adapted to our needs. Following is a brief summary:

1. f is the desired high-resolution image we wish to find. $\{g_k\}_{k=1}^{K}$ are the K acquired low-resolution images. The imaging process is modelled by:

$$g_k = (T_k f) \downarrow s + \eta_k \qquad [1]$$

where T_k is the translation operator that shifts the image, $\downarrow s$ is the downsampling operator, and η_k is noise.

2. An initial guess is generated. In our case, we chose the mean of all the shifted low-resolution images:

$$f^{(0)} = \frac{1}{K}\sum_k T_k^{-1}(g_k \uparrow s) \quad [2]$$

where $\uparrow s$ is an upsampling operator.
3. The low-resolution images that would be acquired if the guess were correct are estimated for $k = 1..K$:

$$g_k^{(0)} = (T_k f^{(0)}) \downarrow s \quad [3]$$

and a new guess is generated:

$$f^{(1)} = f^{(0)} + \frac{1}{K}\sum_{k=1}^{K} T_k^{-1}((g_k - g_k^{(0)}) \uparrow s). \quad [4]$$

For the upsampling operator at this stage, we used bilinear interpolation. This smoothing step was important for keeping the SNR at acceptable levels.
4. The process is repeated iteratively to minimize an error function consisting of the mean squared difference between the original images, $\{g_k\}$, and the estimated low-resolution images at step n, $\{g_k^{(n)}\}$.

Most superresolution algorithms require knowledge of a space-invariant blurring operator or point spread function (PSF). In echo planar imaging, if one ignores spatial distortions, the PSF is negligible in the read-out direction, and dependent on T_2^* and the effective bandwidth in the phase-encode direction. The full width at half maximum (FWHM) of the PSF in the phase-encode direction is $2T/(\pi T_2^*)$ pixels wide where T is the total acquisition time for one slice. If we assume a value for T_2^* in the brain of approximately 70 msec at 1.5 Tesla, the FWHM of the PSF with our imaging parameters is approximately one pixel in the low-resolution image. Note that the PSF is in reality space variant, such that this is not a good approximation. There was no noticeable improvement of the image quality when a constant blurring was incorporated into the algorithm.

The convergence condition specified by Irani and Peleg relates to the special case of deblurring of an image through superresolution methods, i.e., does not encompass situations in which images are upsampled. For 2D translations the convergence condition is:

$$\|\delta - h*p\|_2 < 1 \quad [5]$$

where δ is the unity pulse function, h is the PSF, and p is a "back-projection" kernel. Our implementation of the algorithm, with $p = \delta$, and with the above estimate of the PSF, fulfills this convergence condition. The validity of this calculation in our case remains to be shown, but so far we have always experienced very fast convergence.

Anisotropy Calculation

For each voxel, the 3×3 diffusion tensor, **D**, is found from the equation shown in Eq. [6], using the intensities of the voxel in each of the nine images, S, and the corresponding gradient vector that was applied, **G** (4).

$$\ln S = \ln S_0 - \gamma^2\delta^2(\Delta - \delta/3)\mathbf{GDG}^T \quad [6]$$

γ is the gyromagnetic ratio of ^{1}H, δ is the duration of the diffusion sensitizing gradient pulses, and Δ is the time between the centers of the two gradient pulses. The diffusion weighting is usually specified in terms of the factor b given by $b = (\gamma\delta G)^2(\Delta - \delta/3)$.

Determination of an index of anisotropy is a way of reducing the diffusion tensor data to one value per pixel, which can then be straightforwardly displayed as an image. For commonly used indices and an excellent analysis of DTI in biological tissue, see Basser and Pierpaoli (4). We chose to derive an index from a set of geometrically intuitive measures of anisotropy (presented in Refs. 12 and 26) that differentiate between diffusion that has linear, planar, or spherical spatial characteristics. The linear, planar, and spherical measures are given in Eq. [7].

$$C_l = \frac{\lambda_1 - \lambda_2}{\lambda_1 + \lambda_2 + \lambda_3},\ C_p = \frac{2(\lambda_2 - \lambda_3)}{\lambda_1 + \lambda_2 + \lambda_3},\ C_s = \frac{3\lambda_3}{\lambda_1 + \lambda_2 + \lambda_3} \quad [7]$$

where $\lambda_{1,2,3}$ are the eigenvalues of the diffusion tensor in descending order of magnitude. An index of anisotropy is derived, C_a, that is high in voxels that exhibit at least one direction of relatively restricted diffusion:

$$C_a = C_l + C_p = \frac{\lambda_1 + \lambda_2 - 2\lambda_3}{\lambda_1 + \lambda_2 + \lambda_3}. \quad [8]$$

A measure we find suitable for fiber tract delineation is C_t given in Eq. [9]:

$$C_t = C_l + \frac{1}{2}C_p = \frac{\lambda_1 - \lambda_3}{\lambda_1 + \lambda_2 + \lambda_3}. \quad [9]$$

Using this index, voxels that exhibit pure planar diffusion have half the intensity of voxels exhibiting pure linear diffusion. All of the measures C_l, C_p, C_s, C_a, and C_t lie in the range [0,1].

RESULTS

Simulation

A high-SNR, high-resolution (256×256 0.94 mm in-plane) image was shifted and contracted so as to create eight images (128×64) corresponding to the experimental paradigm. Gaussian random noise was added to the low-resolution images to give them an added SNR of 12—the same as that of the experimental diffusion-weighted images. Part of one of the low-resolution shifted images with noise added is shown in Fig. 2a.

An initial guess was generated from addition of the eight shifted images, shown in Fig. 2b. The reconstructed image after seven iterations is shown in Fig. 2c. The original image with the same amount of noise added is shown for comparison in Fig. 2d. Figure 2e–h shows the same procedure fol-

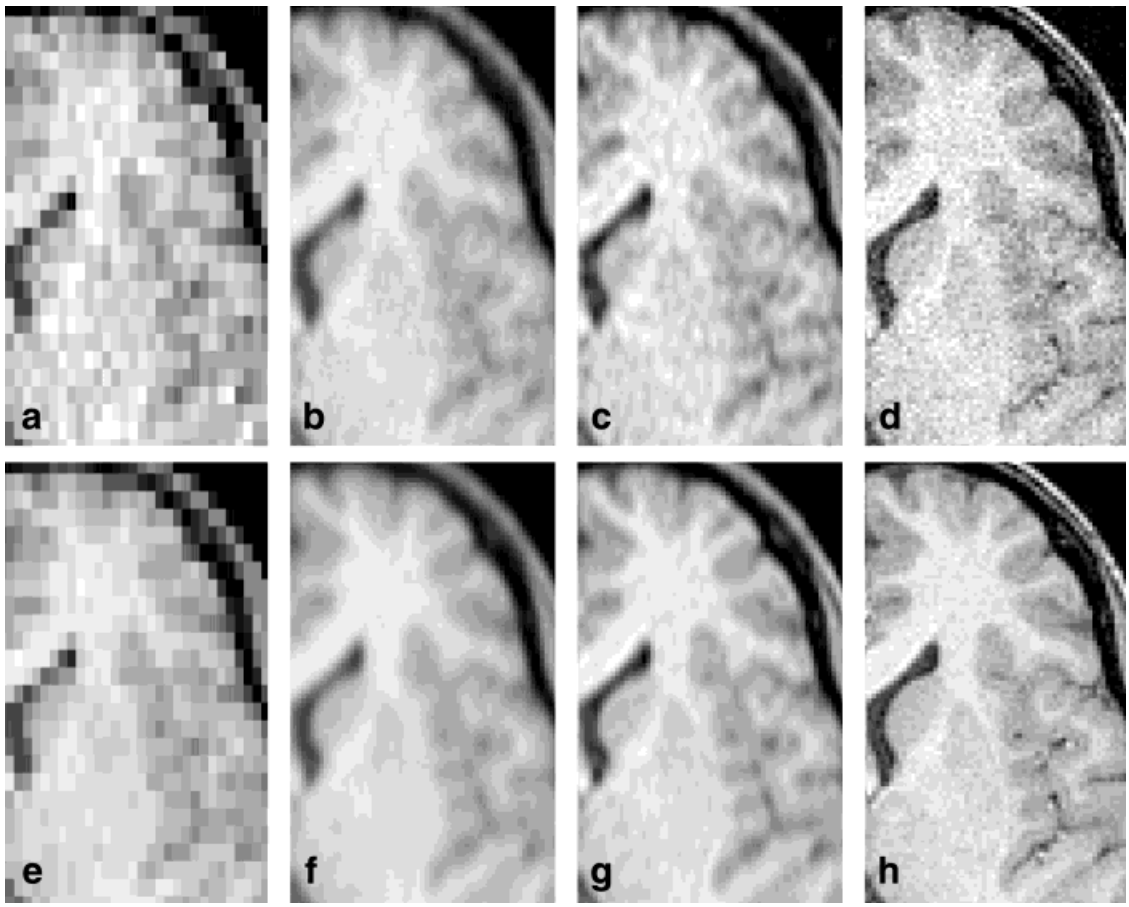

FIG. 2. Results of simulation with noise. **a** has SNR of 12; **e** has SNR of 36; **b** and **f** is the first guess obtained from combining the low-resolution images; **c** and **g** show the final result of the algorithm; **d** and **h** the original images + noise for comparison.

lowed for images with an initial SNR of 36. The improvement in resolution is clear, as is the detrimental effect of noise.

Phantom Imaging

Phantom studies yielded the images in Fig. 3. Figure 3a shows one of the original 64 × 64 resolution images. The end result of the superresolution method is shown in Fig. 3b. For this phantom, we reduced the FOV, changing the pixel dimensions from 2 mm × 4 mm to 2.2 mm × 2.2 mm. Four shifted images were acquired in order to reconstruct a superresolution image with nominal resolution of 128 × 128. The structure of the comb in the upper left corner of the image is clearer in the superresolution image.

Brain Imaging

For each slice 72 images were acquired: eight shifted images for each of nine diffusion weightings. Figure 4 shows the improvement obtained in one of the images ($b = 1000$ sec/mm^2). The SNR of the final images depends on the

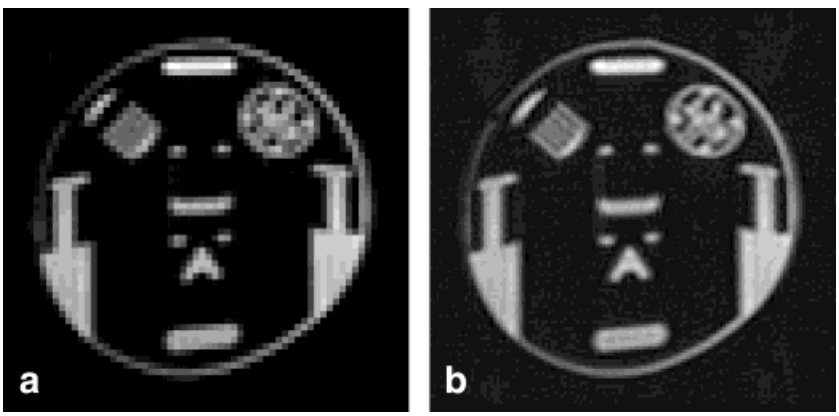

FIG. 3. **a:** Acquired phantom image 64 × 64; **b:** reconstructed superresolution image 128 × 128.

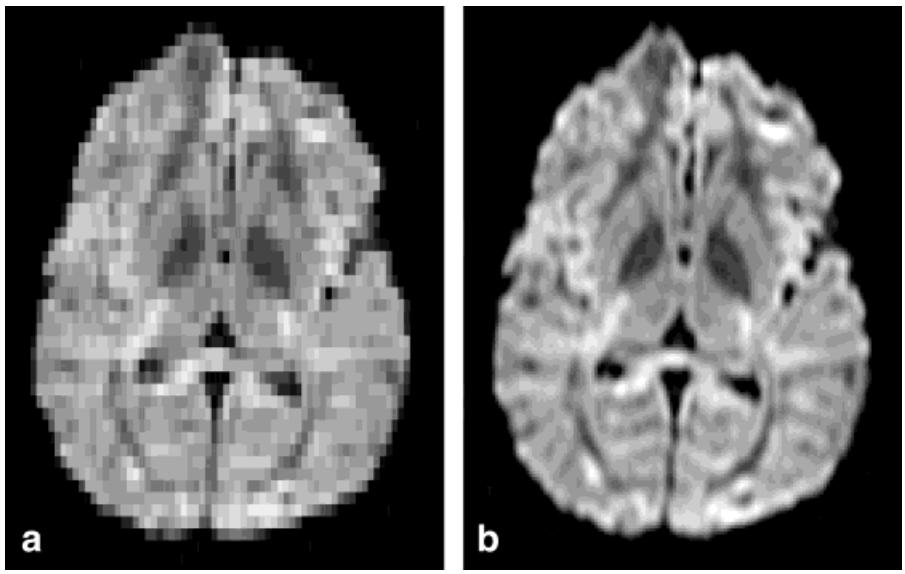

FIG. 4. **a:** One of the acquired diffusion-weighted images; **b:** reconstructed superresolution image.

smoothing method used in the upsampling operator. In our implementation, the SNR of the high-resolution image in Fig. 4b is approximately 20% better than the SNR of the image in Fig. 4a when the latter is interpolated to 256 × 256. The nine reconstructed images were used to calculate the diffusion tensor for each voxel. Figure 5a shows the anisotropy map (index C_a) calculated from one shifted subset of the original low-resolution images after they had been bilinearly interpolated to 256 × 256. Figure 5b shows the anisotropy map calculated from the high-resolution reconstructed images. Much more detail is apparent in the higher-resolution image. The anatomy is shown for reference.

The white matter fiber tract directions are demonstrated in Fig. 6a and b. We display the vector $C_t\hat{\mathbf{e}}_1$ on the background of the corresponding anatomical image, where $\hat{\mathbf{e}}_1$ is the eigenvector corresponding to the largest eigenvalue, λ_1, of the diffusion tensor. The blue headless arrows represent the in-plane components of $C_t\hat{\mathbf{e}}_1$. The out-of-plane components of $C_t\hat{\mathbf{e}}_1$ are shown in colors ranging from green through yellow to red, with red indicating the highest value for this component. See Ref. 12 for some of the limitations of this display method.

The detail in Fig. 6b, created from the superresolution images, is clearly superior to that of Fig. 6a, created from interpolated low-resolution data. We have no absolute information about the true fiber tract orientation, but have found no unexpected results in the reconstructed data. Data from interpolated images are inaccurate in areas with sudden changes in fiber tract direction, which are quite common in the brain.

DISCUSSION

We have presented a robust method for improving the spatial resolution in MRI, applicable in particular to cases where *k*-space segmentation is difficult to achieve. We have shown results for diffusion tensor imaging fiber tract mapping. Increased resolution in DTI enables us to answer questions about the connectivity of the human brain in

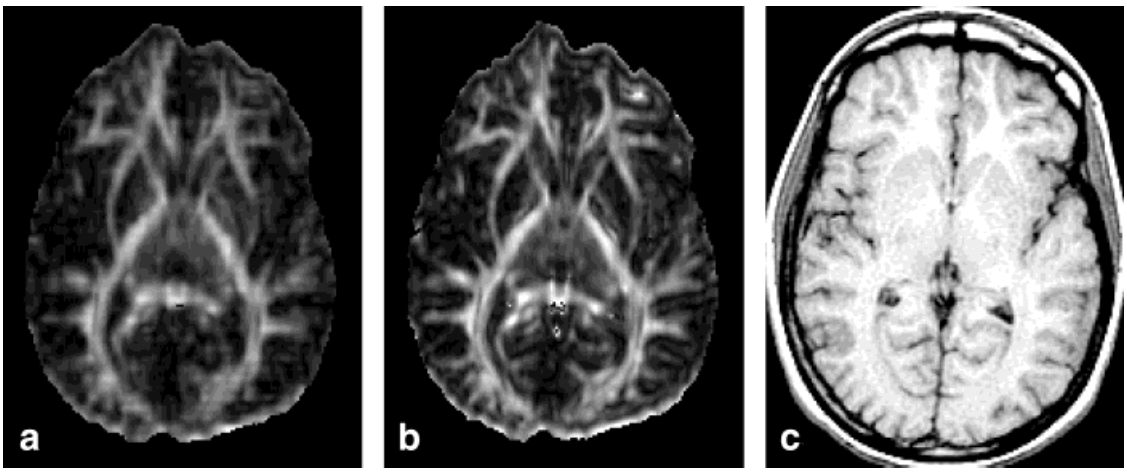

FIG. 5. **a:** Anisotropy map calculated from interpolated low-resolution (128 × 64) images; **b:** anisotropy map calculated from reconstructed superresolution images; **c:** anatomical T_1 for reference. The anisotropy maps are displayed with equal windowing of [0 0.8].

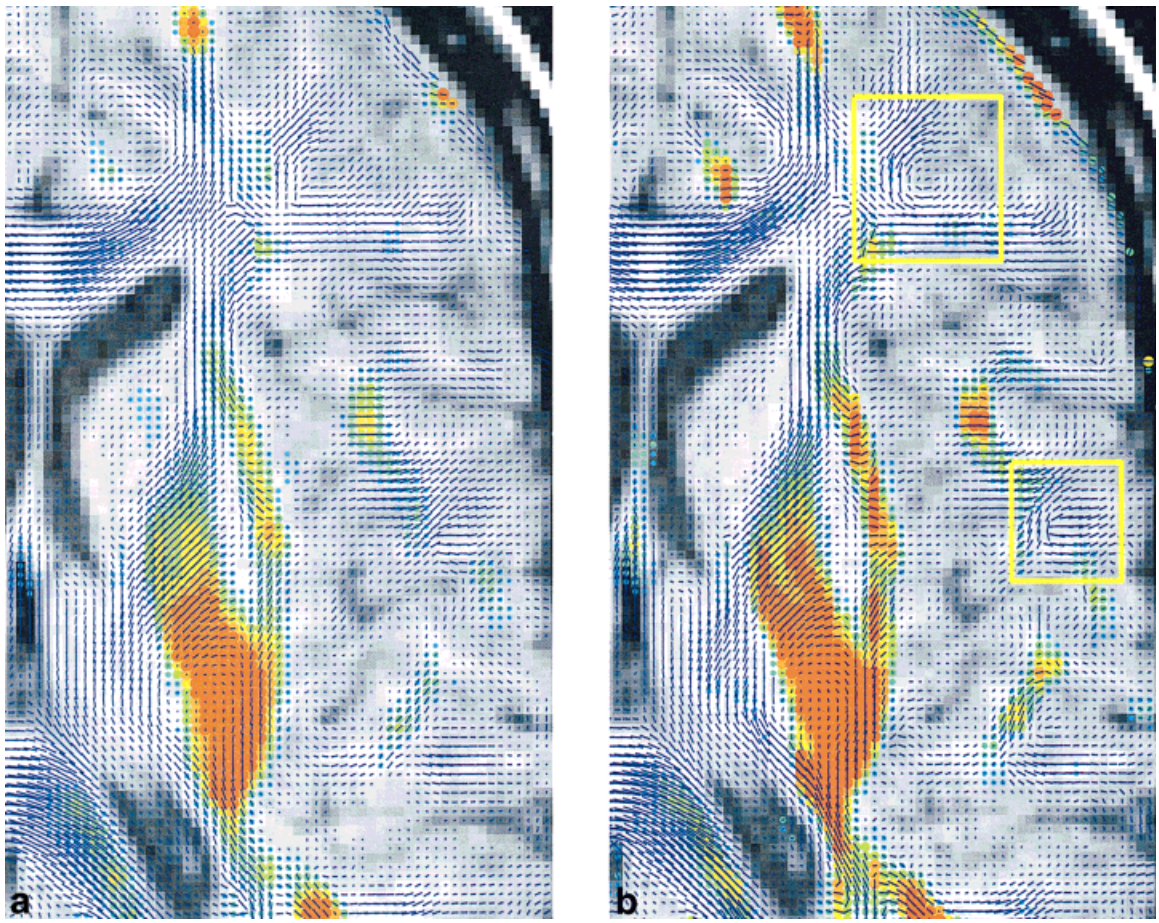

FIG. 6. **a:** White matter fiber tract directions calculated from interpolated low-resolution (128 × 64) images; **b:** tract directions calculated from reconstructed superresolution images. The square frames outline two of the many areas of increased detail compared to **a**. See text for details of the display method.

vivo, giving a valuable tool for both neurosurgical planning and neuroscience research.

Patient motion can in some cases be incorporated into the superresolution algorithm, whereas multishot imaging is practically impossible in the presence of motion. (Superresolution methods were initially developed in the field of computer vision to handle data from moving cameras or moving objects.) The extent of movement can be assessed using image registration techniques, and the true shift of the image, including the subject's motion, can be used in the superresolution algorithm. Three-dimensional superresolution methods with extra image sampling could be implemented to ensure sufficient coverage of sub-pixel areas. There is still much space for optimization of the choice of superresolution algorithm, of the image acquisition strategy, and for the adaptation of one to the other.

ACKNOWLEDGMENTS

We thank C. Le Ninte of GE Medical Systems Europe for providing us with a flexible EPI diffusion sequence, and S. Peleg and A. Zomet for their timely assistance in initial evaluation of the technique. S. Peled received support from the Adams Center for Brain Research, Tel Aviv University.

REFERENCES

1. Moseley ME, Cohen Y, Mintorovitch J, Chileuitt L, Shimizu H, Kucharczyk J, Wendland MF, Weinstein PR. Early detection of regional cerebral ischemia in cats: comparison of diffusion- and T_2-weighted MRI and spectroscopy. Magn Reson Med 1990;14:330–346.
2. Hacke W, Warach S. Diffusion-weighted MRI as an evolving standard of care in acute stroke. Neurology 2000;54:1548–1549.
3. Chenevert TL, Brunberg JA, Pipe JG. Anisotropic diffusion in human white matter: demonstration with MR techniques in vivo. Radiology 1990;177:401–405.
4. Basser PJ, Mattiello J, Le Bihan D. Estimation of the effective self-diffusion tensor from the NMR spin echo. J Magn Reson B 1994;103: 247–254.
5. Turner R, Le Bihan D, Maier J, Vavrek R, Hedges LK, Pekar J. Echo planar imaging of intravoxel incoherent motions. Radiology 1990;177: 407–414.
6. Hennig J, Nauerth A, Friedburg H. RARE imaging: a fast imaging method for clinical MR. Magn Reson Med 1986;3:823–833.
7. Feinberg DA, Oshio K. GRASE (gradient- and spin-echo) MR imaging: a new fast clinical imaging technique. Radiology 1991;181:597–602.
8. Ordidge RJ, Helpern JA, Qing ZQ, Knight RA, Nagesh V. Correction of motional artifacts in diffusion-weighted MR images using navigator echoes. Magn Reson Imag 1994;12:455–460.
9. Gudbjartsson H, Maier SE, Mulkern RV, Mórocz IÁ, Patz S, Jolesz FA. Line scan diffusion imaging. Magn Reson Med 1996;36:509–519.
10. Glover GH, Pauley JM. Projection reconstruction techniques for reduction of motion effects in MRI. Magn Reson Med 1992;28:275–289.
11. Trouard TP, Theilmann RJ, Altbach MI, Gmitro AF. High resolution diffusion imaging with DIFRAD-FSE (diffusion-weighted radial acquisition of data with fast spin-echo) MRI. Magn Reson Med 1999;42:11–18.

12. Peled S, Gudbjartsson H, Westin C-F, Kikinis R, Jolesz FA. Magnetic resonance imaging shows orientation and asymmetry of white matter fiber tracts. Brain Research 1998;780:27–33.
13. Xue R, van Zijl PCM, Crain BJ, Solaiyappan M, Mori S. In vivo three-dimensional reconstruction of rat brain axonal projections by diffusion tensor imaging. Magn Reson Med 1999;42:1123–1127.
14. Conturo TE, Lori NF, Cull TS, Akbudak E, Snyder AZ, Shimony JS, McKinstry RC, Burton H, Raichle ME. Tracking neuronal fiber pathways in the living human brain. Proc Natl Acad Sci USA 1999;96: 10422–10427.
15. Jones DK, Simmons A, Williams SC, Horsfield MA. Non-invasive assessment of axonal fiber connectivity in the human brain via diffusion tensor MRI. Magn Reson Med 1999;42:37–41.
16. Poupon C, Clark CA, Frouin V, Régis J, Bloch I, Le Bihan D, Mangin J. Regularization of diffusion-based direction maps for the tracking of brain white matter fascicles. Neuroimage 2000;12:184–195.
17. Callaghan PT. Principles of nuclear magnetic resonance microscopy. Oxford Science; 1991.
18. Assaf Y, Cohen Y. Assignment of the water slow-diffusing component in the central nervous system using q-space diffusion MRS: implications for fiber tract imaging. Magn Reson Med 2000;43:191–199.
19. Wedeen VJ, Reese TG, Tuch DS, Weigel MR, Dou J-G, Weiskoff RM, Chessler D. Mapping fiber orientation spectra in cerebral white matter with fourier-transform diffusion MRI. In: Proceedings of the 8th Annual Meeting of ISMRM, Denver, 2000. p 82.
20. Irani M, Peleg S. Motion analysis for image enhancement: resolution, occlusion, and transparency. J Vis Comm Image Rep 1993;4:324–335.
21. Tekalp AM, Ozkan MK, Sezan MI. High resolution image reconstruction for lower resolution image sequences and space-varying image restoration. IEEE International conference on acoustics, speech, and signal processing (San Francisco, CA), March 23–26:III-169–172, 1992.
22. Huang TS, Tsai RY. Multi-frame image restoration and registration, vol. 1. JAI Press Inc.; 1984. p 317–339.
23. Kim SP, Bose NK, Valenzuela HM. Recursive reconstruction of high resolution image from noisy undersampled multiframes. IEEE Transactions on Acoustics Speech and Signal Processing 1990;38:1013–1027.
24. Ur H, Gross D. Improved resolution from subpixel shifted pictures. CVGIP: Graphical Models and Image Processing 1992;54:181–186.
25. Pierpaoli C, Jezzard P, Basser PJ, Barnett A, Di Chiro G. Diffusion tensor MR imaging of the human brain. Radiology 1996;201:637.
26. Westin C-F, Peled S, Gudbjartsson H, Kikinis R, Jolesz FA. Geometrical diffusion measures for MRI from tensor basis analysis. In: Proceedings of the 5th Annual Meeting of ISMRM, Vancouver, Canada, 1997. p 1742.